Dynamic Overmodulation Scheme for Improved Current Regulation in PMSM Drives

Jiwon Yoo, *Student Member*, *IEEE*, and Seung-Ki Sul, *Fellow*, *IEEE*

***Abstract*— The overmodulation scheme plays an essential role in the dynamic performance of the current regulation under voltage limitation. This paper analyses how the non-linearity of the voltage hexagon affects dynamic overmodulation. Most dynamic overmodulation schemes had considered the voltage hexagon as the limit of the output voltage to maximize the voltage utilization. However, these schemes do not show uniform dynamic performance according to the rotor position on the voltage hexagon. To overcome this limitation, this paper proposes an overmodulation scheme that is robust against the rotor position variation. The computer simulation and experimental results verify that the proposed method has consistent performance regardless of the rotor position with less *d*-axis current overshoot keeping the fast dynamics.**

***Index Terms*— Current regulation, dynamic performance, overmodulation, permanent magnet synchronous motor.**

NOMENCLATURE

$(\,)^{\mathbf{s}}_{\mathbf{dqs}} = \begin{bmatrix} (\,)^{s}_{ds} \\ (\,)^{s}_{qs} \end{bmatrix}$	*dq*-vector variable at stationary reference frame.
$(\,)^{\mathbf{r}}_{\mathbf{dqs}} = \begin{bmatrix} (\,)^{r}_{ds} \\ (\,)^{r}_{qs} \end{bmatrix}$	*dq*-vector variable at rotor reference frame.
$(\,)^{*}$	Reference value.
θ_r	Electrical rotor angle.
ω_r	Electrical rotor speed.
p	Number of pole pairs.

I. INTRODUCTION

PERMANENT magnet synchronous motors (PMSMs) have been widely used for various industry applications, such as servo drives and electric/hybrid vehicles. The fast-dynamic performance is a hallmark of PMSM that those applications require. To exploit the fast and accurate torque response, most PMSM drive systems adopt the closed-loop control structure, i.e., field-oriented-control (FOC). In FOC, the closed-loop current regulator plays an essential role in the desired dynamic performance.

Manuscript received June 29, 2021; revised October 24, 2021 and December 5, 2021; accepted December 26, 2021. This work was supported in part by the Hyundai Motor Chung Mong-Koo Foundation, and in part by the BK 21 FOUR program funded by the Ministry of Education (MOE) of Korea and National Research Foundation (NRF) of Korea. *(Corresponding author: Seung-Ki Sul.)*

Jiwon Yoo and Seung-Ki Sul are with the Department of Electrical and Computer Engineering, Seoul National University, Seoul, 08826, Korea (e-mail: jiwon.yoo@eepel.snu.ac.kr; sulsk@plaza.snu.ac.kr).

The closed-loop current regulator provides satisfactory performance when the output voltage of the current regulator is not saturated. However, the limited dc-link voltage, which comes from the limited battery or grid voltage, interferes with the ideal operation of the current regulator. When the output voltage is saturated, the current regulation capability is severely degraded. To solve this problem, various overmodulation (OVM) schemes have been developed to improve the dynamic performance of PMSM under the output voltage limitation.

Firstly, various research works tried to achieve the maximum voltage utilization [1]-[3]. These methods exploit the near-vertex region of the voltage hexagon to obtain larger fundamental voltage. Although it helps to extend the feasible operating region in the steady-state, it lacks the consideration of the transient situation, where the direction of the voltage vector has an impact on the current regulation. An OVM obsessed with the maximum voltage utilization may shoot a wrongheaded voltage vector to keep the maximum fundamental voltage even in the transient situation.

To overcome this, the OVM schemes considering dynamic operating conditions of PMSM were reported [4]-[9]. In [4] and [5], the voltage reference was interpreted as a sum of effective electromotive force (EMF) and the dynamic voltage, which determines the current variation. And, the output voltage is set by keeping the phase of dynamic voltage. In [6], a similar approach was combined with the maximum voltage utilization. Ref. [7]-[9] had selected the output voltage vector that reduced the current/torque error at every single control period. These methods could improve the dynamic performance by preserving the current tracking performance. However, these strategies were vulnerable to parameter variation. Moreover, chasing the instant current reference does not guarantee the minimum response time for the transient situation.

Many researchers tried to reduce the transient settling time for current reference change. The time-optimal control (TOC) schemes provided an analytical solution for the least transient time under the given voltage limitation [10]-[14]. In [10]-[12], the optimal voltage output was calculated for an ideal PMSM in terms of the settling time. However, these optimal-control-based OVMs require an excessive calculation burden and are still vulnerable to parameter variation. Nevertheless, it is noteworthy that the obtained current trajectory has a negative *d*-axis overshoot in transient. In [13] and [14], similar results were drawn out based on the flux-based analysis. The flux-based optimal control provides a promising performance, but it

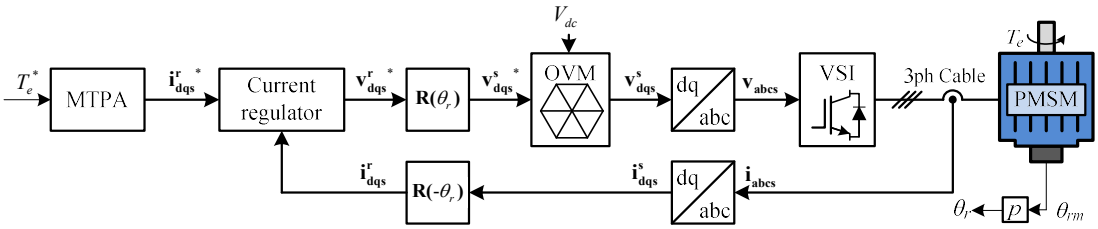

Fig. 1. Control block diagram of PMSM drives

requires a complicated control block, which may not be cooperative with the conventional current regulator.

Kwon *et al*. gave an intuitive analysis for the phenomenon of the negative *d*-axis current overshoot [15]-[16]. In [15], a voltage feedback scheme to reduce *d*-axis current in transient was proposed. Reducing *d*-axis current secures more *q*-axis voltage margin so that the torque response can be improved. In reducing *d*-axis current, the voltage output is inherently ahead of the original voltage reference. In [16], the direct voltage reference modification (VRM) was proposed under the same principle. It modified the voltage reference itself directly instead of changing voltage reference through the current regulator. Furthermore, Yun *et al.* claimed that the VRM could be simply implemented by adjusting offset voltage in pulse width modulation (PWM) [17], [18]. The VRM can provide a quasi-time-optimal dynamic response without the premade look-up-tables (LUTs).

However, *d*-axis current overshoot in time-optimal trajectory may adversely affect the maximum current capability of the inverter and motor. Even if the current overshoot over the current limit lasts only a few milliseconds, it can be fatal for the power devices of the inverter. Moreover, since the current overshoot occurs on the negative *d*-axis, an excessive *d*-axis current may irreversibly demagnetize the permanent magnet of the rotor. Hence, the current overshoot in transients should be predicted and minimized. However, since this phenomenon is intricately intertwined with the voltage hexagon and the OVM schemes, the peak of *d*-axis current overshoot varies depending on the rotor position and the moment where the current reference is changed. The unpredictable *d*-axis current overshoot makes it challenging to set the current rating of the inverter and the feasible region of the system.

This paper analyses the interference of the non-linearity of voltage hexagon on the dynamic performance in the OVM situation. The analysis shows that the larger voltage magnitude sacrificing the leading angle may not be helpful to the dynamic performance. Moreover, the *d*-axis current overshoot highly depends on the angle between the voltage output and the voltage reference. Through the analysis, it is revealed that the consistent current response and the fast dynamic response can be achieved simultaneously, by designing adequate OVM scheme.

In this paper, an OVM scheme with consistent current response is proposed. The proposed OVM keeps the same leading angle between the voltage output and its reference regardless of the rotor position. The consistency in voltage leading angle is accomplished by employing the circumscribed circle of the voltage hexagon in the calculation of the output voltage. And, to inherit the fast response property from VRM methods, the voltage shifting angle is presented. Through the consistent voltage angle advance, the proposed OVM achieves the fast-dynamic performance and the consistent current response simultaneously. Thanks to the proposed OVM, *d*-axis current overshoot can be predicted while keeping the fast-dynamic performance of the current regulation. Furthermore, the *d*-axis current overshoot can be mitigated by adjusting the voltage shifting angle. In an implementation point of view, the proposed OVM scheme has an advantage of being compatible with the conventional current regulator. The feasibility of the proposed method is verified with a series of simulation and experimental tests.

In addition to the previously presented paper [19], this paper provides the following.

1) Analysis of settling time in time-optimal solutions.
2) Detailed analysis of the proposed method.
3) Simulation and experimental results under various operating points.

II. Transient Analysis on Voltage Saturation

A. Voltage Saturation in PMSM Drives

Fig. 1 depicts the control block diagram of PMSM drives. Firstly, the current reference at the rotor reference frame (RRF), $\mathbf{i}^{r*}_{dqs}$, corresponding to the desired torque reference T_e^* is calculated. Under the base speed, the current reference that satisfies the maximum torque per Ampere (MTPA) operation is often selected. The output current at RRF, $\mathbf{i}^{r}_{dqs}$, is regulated to $\mathbf{i}^{r*}_{dqs}$ through the current regulator and the voltage source inverter (VSI). The current regulator calculates the voltage reference at RRF, $\mathbf{v}^{r*}_{dqs}$, to control the current with a desired control bandwidth. Since the VSI synthesizes the output voltage at the stationary reference frame (SRF), $\mathbf{v}^{r*}_{dqs}$ is converted to the voltage reference at SRF, $\mathbf{v}^{s*}_{dqs}$. If $\mathbf{v}^{s*}_{dqs}$ is inside the synthesizable region of VSI, the current control is not interfered, and an exemplary performance can be expected. Otherwise, the OVM block intervenes, and the primitive voltage reference should be modified into one in the feasible region.

The voltage saturation can be categorized with whether the voltage deficiency occurs only in the transient state or persists in the steady-state. In the former case, the voltage saturation is caused by the rapid current reference change, and it can be resolved by selecting the proper OVM scheme. The latter may occur due to an inappropriate current reference under certain operating conditions. In the latter case, the current reference

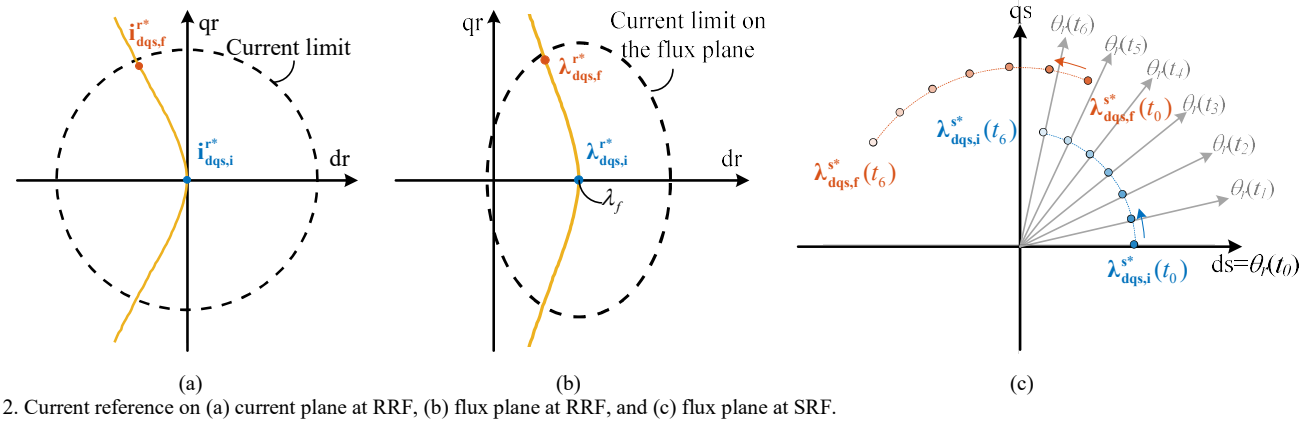

Fig. 2. Current reference on (a) current plane at RRF, (b) flux plane at RRF, and (c) flux plane at SRF.

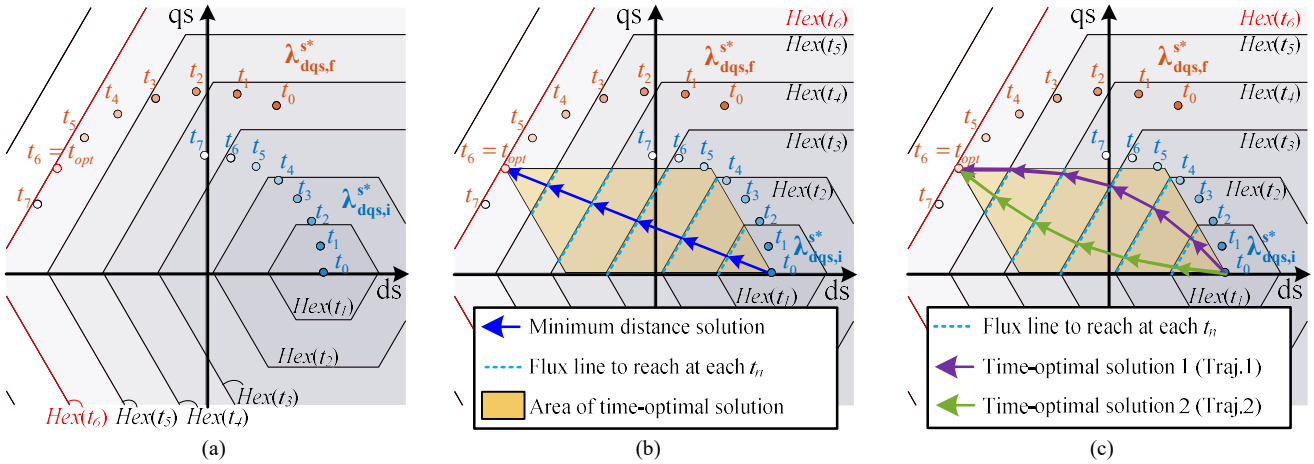

Fig. 3. (a) Reachable flux region at t_n, $Hex(t_n)$. (b) Minimum distance flux trajectory. (c) Various time-optimal solutions.

should be adjusted by additional controllers, e.g., flux-weakening controller, to avoid losing the control stability.

This paper focuses on the voltage deficiency in the transient situation. Thus, it is assumed that the current references are realizable at the steady-state, and the voltage output is saturated by the rapid current reference change.

B. Transient Analysis on the Stationary Reference Frame

In this section, the transients where the current reference varies rapidly are analyzed, and the conditions for fast dynamics and uniform current response will be discussed. If the voltage drop due to stator resistance is neglected in the high-speed region, the voltage equation of PMSM can be expressed as

$$\mathbf{v}_{\mathbf{dqs}}^{\mathbf{s}} = \frac{d}{dt}\boldsymbol{\lambda}_{\mathbf{dqs}}^{\mathbf{s}}, \tag{1}$$

where $\mathbf{v}_{\mathbf{dqs}}^{\mathbf{s}}$ and $\boldsymbol{\lambda}_{\mathbf{dqs}}^{\mathbf{s}}$ are the stator output voltage and flux vector at SRF, respectively. Therefore, the time integral of $\mathbf{v}_{\mathbf{dqs}}^{\mathbf{s}}$ directly represents the stator flux variation in a time interval.

Let's assume a situation that the step torque reference is applied. The current reference at RRF varies from $\mathbf{i}_{\mathbf{dqs,i}}^{\mathbf{r}*}$ to $\mathbf{i}_{\mathbf{dqs,f}}^{\mathbf{r}*}$, as shown in Fig. 2(a). The subscripts 'i' and 'f' stand for the initial and final reference values, respectively. It is assumed that $\mathbf{i}_{\mathbf{dqs,i}}^{\mathbf{r}*}$ and $\mathbf{i}_{\mathbf{dqs,f}}^{\mathbf{r}*}$ are both on the MTPA line, which is depicted with the yellow line. In addition, it is assumed that they are both the realizable currents under the given operating conditions. Hence, no flux weakening operation is required after reaching $\mathbf{i}_{\mathbf{dqs,f}}^{\mathbf{r}*}$.

Meanwhile, a current vector of PMSM, $\mathbf{i}_{\mathbf{dqs}}^{\mathbf{r}}$, can be mapped to the flux plane, as follows.

$$\boldsymbol{\lambda}_{\mathbf{dqs}}^{\mathbf{r}} = \begin{bmatrix} L_{ds} & 0 \\ 0 & L_{qs} \end{bmatrix} \mathbf{i}_{\mathbf{dqs}}^{\mathbf{r}} + \begin{bmatrix} \lambda_f \\ 0 \end{bmatrix}, \tag{2}$$

where L_{ds} and L_{qs} stand for the static dq-axes inductances and λ_f for the flux linkage of the permanent magnet. The flux variation due to spatial harmonics and cross saturation is neglected for ease of explanation, and the average flux is only considered. Therefore, $\mathbf{i}_{\mathbf{dqs,i}}^{\mathbf{r}*}$ and $\mathbf{i}_{\mathbf{dqs,f}}^{\mathbf{r}*}$ correspond to stator fluxes on RRF, $\boldsymbol{\lambda}_{\mathbf{dqs,i}}^{\mathbf{r}*}$ and $\boldsymbol{\lambda}_{\mathbf{dqs,f}}^{\mathbf{r}*}$ in Fig. 2(b), respectively. In Fig. 2(b), the current limit is depicted as an oval shape on the flux plane considering the saliency of the interior PMSM (IPMSM).

A stator flux at RRF, $\boldsymbol{\lambda}_{\mathbf{dqs}}^{\mathbf{r}}$, can be expressed at SRF as follows.

$$\boldsymbol{\lambda}_{\mathbf{dqs}}^{\mathbf{s}} = \mathbf{R}(\theta_r)\boldsymbol{\lambda}_{\mathbf{dqs}}^{\mathbf{r}}, \tag{3}$$

where

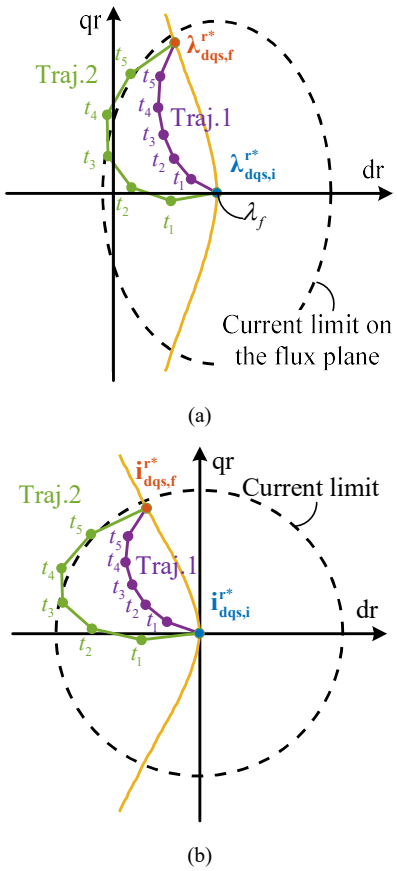

Fig. 4. Current response trajectories on (a) flux plane at RRF and (b) current plane at RRF.

$$\mathbf{R}(\theta_r)=\begin{bmatrix}\cos(\theta_r) & -\sin(\theta_r)\\ \sin(\theta_r) & \cos(\theta_r)\end{bmatrix}. \tag{4}$$

Hence, $\boldsymbol{\lambda}^{r*}_{dqs,i}$ and $\boldsymbol{\lambda}^{r*}_{dqs,f}$ also can be interpreted at SRF, and they would be rotating vectors with the speed of ω_r. Fig. 2(c) shows the rotating flux vectors, $\boldsymbol{\lambda}^{s*}_{dqs,i}(t_n)$ and $\boldsymbol{\lambda}^{s*}_{dqs,f}(t_n)$, according to the time variation, t_0-t_6. $\theta_r(t_n)$ denotes the rotor position at t_n. As shown in (1), $\mathbf{v}^{s}_{dqs}$ determines the stator flux variation so that the proper voltage vector should be selected to chase the rotating reference flux $\boldsymbol{\lambda}^{r*}_{dqs,f}$ in a transient situation.

Since an arbitrary voltage vector in the voltage hexagon can be applied in each time period, the reachable flux region at t_n can be drawn by extending the voltage hexagon, as shown in Fig. 3(a). Therefore, the reachable flux region forms a hexagon, $Hex(t_n)$, whose length of one side is $2/3\cdot V_{dc}\cdot(t_n-t_0)$. For the current to be reached $\mathbf{i}^{r*}_{dqs,f}$ in the time of t_n, $\boldsymbol{\lambda}^{s*}_{dqs,f}(t_n)$ should be inside of $Hex(t_n)$. For example, in Fig. 3(a), the minimum settling time T_{min} cannot be less than (t_6-t_0), since $\boldsymbol{\lambda}^{s*}_{dqs,f}(t_1)$ - $\boldsymbol{\lambda}^{s*}_{dqs,f}(t_5)$ are not inside of $Hex(t_0)$-$Hex(t_5)$, respectively. $Hex(t_6)$ finally contains $\boldsymbol{\lambda}^{s*}_{dqs,f}(t_6)$, and the settling moment t_{opt} will be around t_6.

Of course, only a certain sequence of voltage vectors can achieve the minimum settling time. In this paper, these sequences of voltage vectors are denoted by the time-optimal solution. The easiest way to make the stator flux reach $\boldsymbol{\lambda}^{s*}_{dqs,f}$ at t_{opt} is the minimum distance solution, as depicted with the blue arrows in Fig. 3(b). From t_0 to t_{opt}, the minimum distance solution keeps its direction at SRF, taking the shortcut to $\boldsymbol{\lambda}^{s*}_{dqs,f}(t_{opt})$. In addition, the voltage reference in each period should be on the edge of the voltage hexagons.

However, it should be noted that the minimum distance solution is not the unique trajectory for the minimum settling time. Any voltage vector which makes the stator flux reach the light blue dashed line at each time interval can be a time-optimal solution. The orange parallelogram shows the feasible area of time-optimal solutions. The area for the time-optimal solutions can be drawn by stretching the adjacent two vertices of voltage hexagon, and the corners of the parallelogram form 60°. The plurality of the time-optimal solution comes from that the voltage limit forms the hexagon, not a circle.

For example, Fig. 3(c) shows the two different time-optimal solutions, named as Traj.1 and Traj.2. Traj.1, denoted by the purple arrows, represents one of the outward convex time-optimal solutions, and Traj.2, the green arrows, represents one of the inward convex time-optimal solutions. Both can reach $\boldsymbol{\lambda}^{s*}_{dqs,f}$ at t_{opt}, but their current trajectories are contrasting. When the flux vector at SRF is $\boldsymbol{\lambda}^{s}_{dqs}(t_n)$ at t_n, the flux at RRF can be expressed as

$$\boldsymbol{\lambda}^{r}_{dqs}(t_n)=\mathbf{R}\left(-\theta_r(t_n)\right)\boldsymbol{\lambda}^{s}_{dqs}(t_n). \tag{5}$$

Fig. 4(a) depicts the flux trajectory of Traj.1 and Traj.2 on the flux plane at RRF. Even though their settling time is the same, Traj.2 has more d-axis flux overshoot in transients. When the flux vector at RRF is $\boldsymbol{\lambda}^{r}_{dqs}(t_n)$ at t_n, the current vector at RRF can be calculated as

$$\mathbf{i}^{r}_{dqs}(t_n)=\begin{bmatrix}1/L_{ds} & 0\\ 0 & 1/L_{qs}\end{bmatrix}\left(\boldsymbol{\lambda}^{r}_{dqs}(t_n)-\begin{bmatrix}\lambda_f\\ 0\end{bmatrix}\right). \tag{6}$$

Fig. 4(b) shows the calculated current trajectories at RRF. As shown in Fig. 4(b), the flux overshoot directly corresponds to the current overshoot in transients. Subsequently, Traj.2 has an excessive d-axis current overshoot in transients. In short, even though there is a variety of time-optimal solutions, each solution has a different current trajectory. Hence, a trajectory resulting in an excessive d-axis current overshoot should be avoided, even though it is one of the time-optimal solutions.

C. *Calculation of T_{min} for Time-Optimal Solution*

Before further analysis, the range of T_{min} should be confirmed. If the required time for a time-optimal solution is more than half of the rotation period of PMSM, π/ω_r, the area for the time-optimal solution would be excessively far from the current regulator output, and the validity of the previous analysis may not be held. Hence, the required time for the time-optimal solution, i.e., T_{min}, should be calculated.

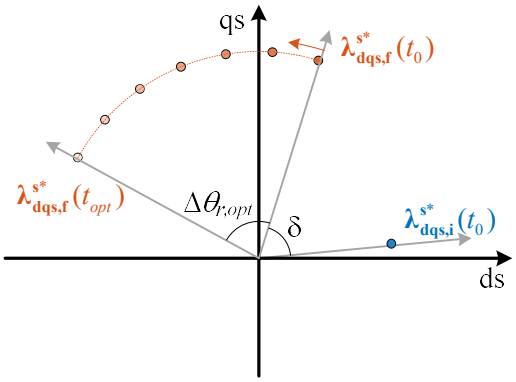

Fig. 5. Vector diagram of time-optimal solution.

Fig. 5 shows the vector diagram of $\boldsymbol{\lambda}^{s*}_{dqs,i}$ and $\boldsymbol{\lambda}^{s*}_{dqs,f}$. From t_0 to t_{opt}, the rotor would rotate as much as $\Delta\theta_{r,opt}=\omega_r \cdot T_{min}$. The letter 'δ' in Fig. 5 denotes the angle difference between $\boldsymbol{\lambda}^{s*}_{dqs,i}(t_0)$ and $\boldsymbol{\lambda}^{s*}_{dqs,f}(t_0)$. Since it has been assumed that current references are realizable under given operating conditions, the following inequalities can be deduced under space-vector PWM (SVPWM).

$$\omega_r \| \boldsymbol{\lambda}^{s*}_{dqs,f} \| < \frac{1}{\sqrt{3}} V_{dc}, \tag{7}$$

$$\omega_r \| \boldsymbol{\lambda}^{s*}_{dqs,i} \| < \frac{1}{\sqrt{3}} V_{dc}. \tag{8}$$

$V_{dc}/\sqrt{3}$ is the radius of the inscribed circle of the voltage hexagon. Since the minimum distance solution is one of the time-optimal solutions, the following inequality can be derived.

$$\frac{1}{\sqrt{3}} V_{dc} \cdot T_{min} \le \left\| \mathbf{R}(\omega_r \cdot T_{min}) \boldsymbol{\lambda}^{r*}_{dqs,f} - \boldsymbol{\lambda}^{r*}_{dqs,i} \right\| \le \frac{2}{3} V_{dc} \cdot T_{min}. \tag{9}$$

Solving (9), an upper bound of $\Delta\theta_{r,opt}$ can be obtained as

$$\Delta\theta_{r,opt} < 2. \tag{10}$$

The detailed derivation process of (10) is described in APPENDIX. In conclusion, T_{min} does not exceed $2/\omega_r$, which is less than half of the rotation period.

D. *Effect of Voltage Angle Shift in Current Regulator*

Based on the analysis in the previous section, the behavior of the current regulator under the voltage output saturation can be interpreted. Fig. 6 depicts the block diagram of the current regulator, which consists of a proportional-integral (PI) controller, overmodulation block, and anti-windup controller. Before the current reference change, the voltage reference of the current regulator, $\mathbf{v}^{r*}_{dqs}$, can be expressed as follows, assuming the steady-state.

$$\mathbf{v}^{r*}_{dqs}(t) \approx \omega_r \mathbf{J} \boldsymbol{\lambda}^{r}_{dqs,i}, \tag{11}$$

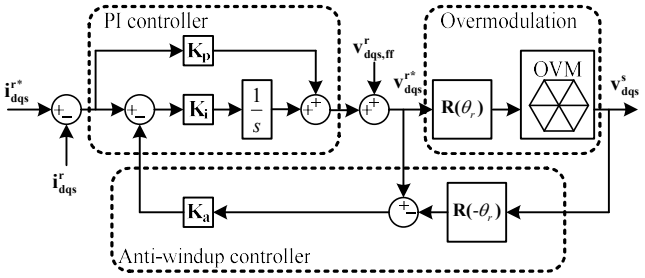

Fig. 6. Block diagram of current regulator.

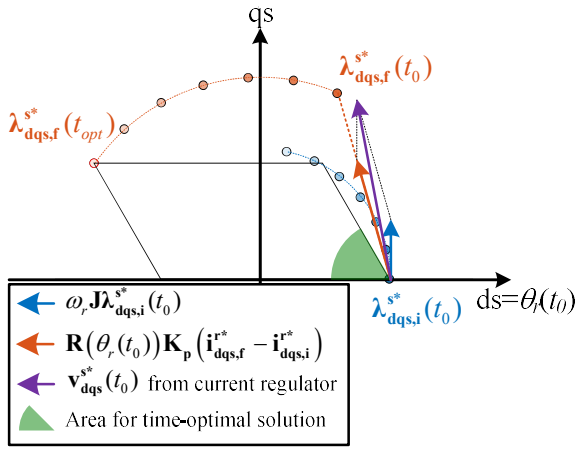

Fig. 7. Direction of voltage reference at t_0.

where $t<t_0$. The matrix $\mathbf{J}$ denotes the rotation matrix with 90°, i.e., $\begin{bmatrix} 0 & -1 \\ 1 & 0 \end{bmatrix}$. At the moment of the current reference change, the proportional controller in the current regulator will react immediately. Thus, the voltage reference from the current regulator can be approximated as follows.

$$\mathbf{v}^{r*}_{dqs}(t_0) \approx \mathbf{K}_p \left(\mathbf{i}^{r*}_{dqs,f} - \mathbf{i}^{r*}_{dqs,i} \right) + \omega_r \mathbf{J} \boldsymbol{\lambda}^{r}_{dqs,i}, \tag{12}$$

where

$$\mathbf{K}_p = \begin{bmatrix} L_{ds}\omega_c & 0 \\ 0 & L_{qs}\omega_c \end{bmatrix}. \tag{13}$$

In (13), ω_c stands for the bandwidth of the current regulator [20]. As the current reference changes more rapidly, the magnitude of $\mathbf{v}^{r*}_{dqs}$ would increase. And, if $\mathbf{v}^{r*}_{dqs}$ exceeds the voltage limit, the overmodulation scheme limits the voltage output inside the voltage hexagon. During the OVM, the integral controller in the current regulator is halted by the anti-windup controller to avoid the windup phenomenon after the voltage saturation. Therefore, during the overmodulation, only the proportional controller intervenes in $\mathbf{v}^{r*}_{dqs}$ calculation.

From (11) and (12), the voltage diagram can be drawn as Fig. 7. It should be noted that $\mathbf{K}_p(\mathbf{i}^{r*}_{dqs,f} - \mathbf{i}^{r*}_{dqs,i})$ is nothing but $\omega_c(\boldsymbol{\lambda}^{r*}_{dqs,f} - \boldsymbol{\lambda}^{r*}_{dqs,i})$, ignoring the inductance mismatch in current regulator gains. Thus, the direction of $\mathbf{v}^{s*}_{dqs}(t_0)$ will be the purple arrow, which is between $\mathbf{K}_p(\mathbf{i}^{r*}_{dqs,f} - \mathbf{i}^{r*}_{dqs,i})$ and $\omega_r \mathbf{J}\boldsymbol{\lambda}^{s*}_{dqs,i}(t_0)$.

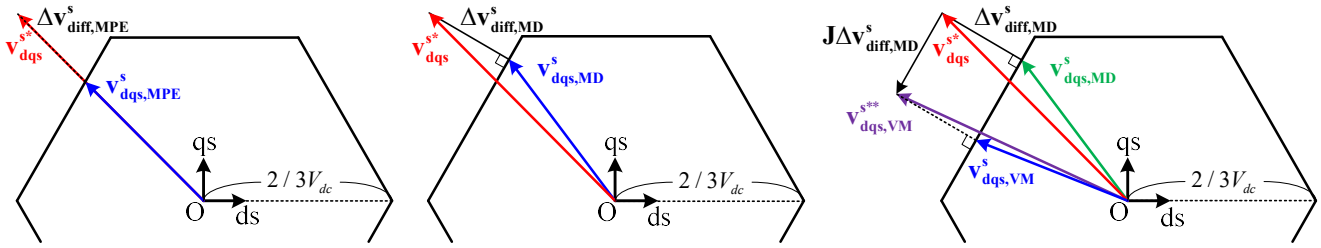

Fig. 8. Various OVM methods. (a) MPE OVM. (b) MD OVM. (c) VM OVM.

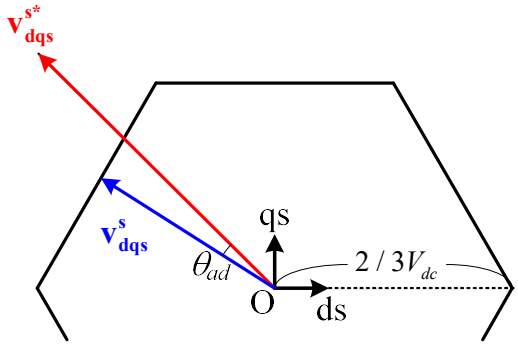

Fig. 9. Phase shift between $\mathbf{v}^{s}_{dqs}$ and $\mathbf{v}^{s*}_{dqs}$, θ_{ad}.

However, for the time-optimal solution, the output voltage should be set inside the green-shaded area. Therefore, an overmodulation scheme setting the output voltage ahead of the original voltage reference can be effective in reducing the settling time.

III. Proposed Angle Shift Overmodulation

A. Conventional Overmodulation Schemes

Based on the analysis in the previous section, the dynamic performance of the conventional overmodulation schemes can be discussed. Among the various OVM strategies, the minimum distance (MD) OVM, the minimum phase error (MPE) OVM, and the voltage reference modification in [16] (VM OVM) are introduced in Fig. 8(a)-(c). MPE OVM and MD OVM are selected to represent the commonly used static OVM methods, and VM OVM represents the VRM methods, which have a fast dynamic performance.

Fig. 8(a) depicts MPE OVM, which preserves the direction of $\mathbf{v}^{s*}_{dqs}$. The output voltage $\mathbf{v}^{s}_{dqs,MPE}$ is calculated by limiting the voltage magnitude to an edge of the voltage hexagon. On the other hand, MD OVM depicted in Fig. 8(b) tries to minimize the magnitude of voltage deficiency $\Delta \mathbf{v}^{s}_{diff,MD}$. Hence, the output voltage $\mathbf{v}^{s}_{dqs,MD}$ is determined as the foot of the perpendicular from $\mathbf{v}^{s*}_{dqs}$ to the voltage hexagon. In this paper, for the sake of simplicity, calculations of MPE OVM and MD OVM are denoted by MPE(*) and MD(*), as follows.

$$\mathbf{v}^{s}_{dqs,MPE} = \mathrm{MPE}\left(\mathbf{v}^{s*}_{dqs}\right), \tag{14}$$

$$\mathbf{v}^{s}_{dqs,MD} = \mathrm{MD}\left(\mathbf{v}^{s*}_{dqs}\right). \tag{15}$$

Unlike MPE and MD OVM, VM OVM has an additional process to improve the transient performance, which is, so-called, voltage reference modification. Even though VM OVM was implemented with Bolognani's OVM [2] in the original literature [16], it can be combined with other OVM methods. In Fig. 8(c), VM OVM combined with MD method is depicted for ease of explanation. In VM OVM, the voltage difference in MD OVM, $\Delta \mathbf{v}^{s}_{diff,MD}$, is calculated as

$$\Delta \mathbf{v}^{s}_{diff,MD} = \mathbf{v}^{s*}_{dqs} - \mathrm{MD}\left(\mathbf{v}^{s*}_{dqs}\right). \tag{16}$$

The modified voltage reference $\mathbf{v}^{s**}_{dqs}$ is obtained by adding $\mathbf{J}\Delta \mathbf{v}^{s}_{diff,MD}$ to $\mathbf{v}^{s*}_{dqs}$. The final voltage output $\mathbf{v}^{s}_{dqs,VM}$ is calculated by applying MD OVM to $\mathbf{v}^{s**}_{dqs}$. In Fig. 8(c), it is assumed that the motor rotates counterclockwise. For the clockwise rotation, $-\mathbf{J}\Delta \mathbf{v}^{s}_{diff,MD}$ should be added instead of $\mathbf{J}\Delta \mathbf{v}^{s}_{diff,MD}$. Consequently, the final voltage output $\mathbf{v}^{s}_{dqs,VM}$ can be expressed as

$$\mathbf{v}^{s}_{dqs,VM} = \mathrm{MD}(\mathbf{v}^{s*}_{dqs} + \mathrm{sgn}(\omega_r)\mathbf{J}\Delta \mathbf{v}^{s}_{diff,MD}), \tag{17}$$

where

$$\mathrm{sgn}(x) = \begin{cases} 1, & \text{for } x \geq 0, \\ -1, & \text{for } x < 0. \end{cases} \tag{18}$$

To analyze the phase of the output voltage in each OVM, θ_{ad} that is the angle between $\mathbf{v}^{s}_{dqs}$ and $\mathbf{v}^{s*}_{dqs}$ is defined as depicted in Fig. 9. When θ_{ad} is positive, $\mathbf{v}^{s}_{dqs}$ is ahead of $\mathbf{v}^{s*}_{dqs}$. In most OVM schemes, θ_{ad} can be represented as a function of $\mathbf{v}^{s*}_{dqs}$. Since the MPE OVM preserves the phase of the voltage reference, there is no voltage angle advance regardless of the rotor position. Thus, θ_{ad} in MPE OVM is null regardless of $\mathbf{v}^{s*}_{dqs}$.

In the case of MD OVM, the voltage phase varies according to $\mathbf{v}^{s*}_{dqs}$. Fig. 10(a) depicts θ_{ad} in MD OVM according to $\mathbf{v}^{s*}_{dqs}$. In MD OVM, θ_{ad} varies slightly around null according to the $\mathbf{v}^{s*}_{dqs}$ variation. For the same magnitude of $\mathbf{v}^{s*}_{dqs}$, θ_{ad} swings from negative to positive values, and their average is zero. Therefore, MD OVM would not provide a significant voltage angle advance in the transient situation.

On the other hand, θ_{ad} in VM OVM is depicted in Fig. 10(b). Since VM OVM intentionally sets the output voltage ahead of

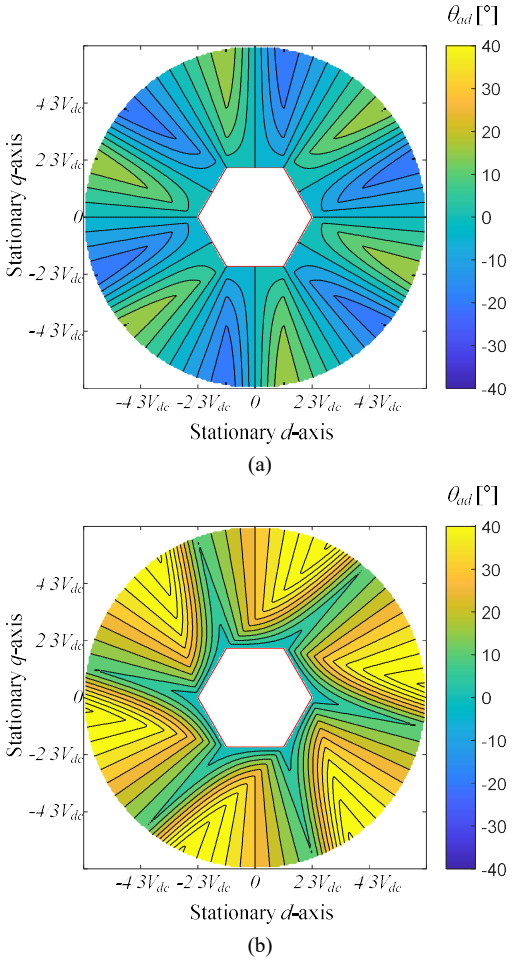

Fig. 10. θ_{ad} according to $\mathbf{v}_{\mathbf{dqs}}^{\mathbf{s}*}$. (a) MD OVM. (b) VM OVM.

the original voltage reference, VM OVM provides always a positive θ_{ad} in OVM region. However, in the calculation of $\mathbf{v}_{\mathbf{dqs}}^{\mathbf{s}**}$, the edges of the voltage hexagon is utilized, and θ_{ad} varies according to the phase of $\mathbf{v}_{\mathbf{dqs}}^{\mathbf{s}*}$ even under the same magnitude of $\mathbf{v}_{\mathbf{dqs}}^{\mathbf{s}*}$. This irregular voltage shift would result in the nonuniform current response in transients.

B. Proposed Overmodulation Scheme

In Section II., the following points have been discussed.

1) For the time-optimal solution, the output voltage should be advanced than the original voltage reference in the case of the current reference change in a step manner.
2) In the transient situation, the direction of the output voltage, rather than its magnitude, plays a crucial role in the current trajectory.

Based on the observation, an OVM scheme with consistent angle shift (AS OVM) can be constructed. To avoid the inherent irregular angle variation of MD OVM or Bolognani's OVM [3], the proposed scheme utilizes MPE OVM in Fig. 8(a). Fig. 11 describes the proposed AS OVM. First, $\mathbf{v}_{\mathbf{dqs,O}}^{\mathbf{s}}$ is calculated by limiting $\mathbf{v}_{\mathbf{dqs}}^{\mathbf{s}*}$ to the circumscribed circle of the voltage hexagon $V_{lim,O}$, whose radius is $2/3 \cdot V_{dc}$. $\mathbf{v}_{\mathbf{dqs,O}}^{\mathbf{s}}$ can be calculated as

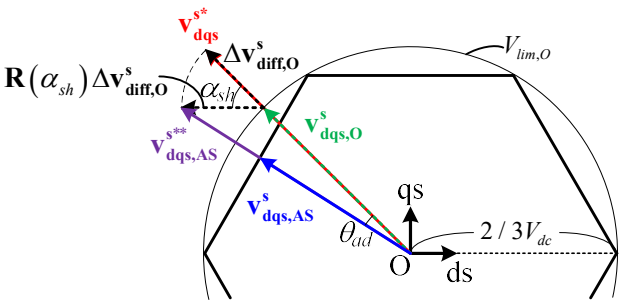

Fig. 11. Voltage diagram of the proposed AS OVM.

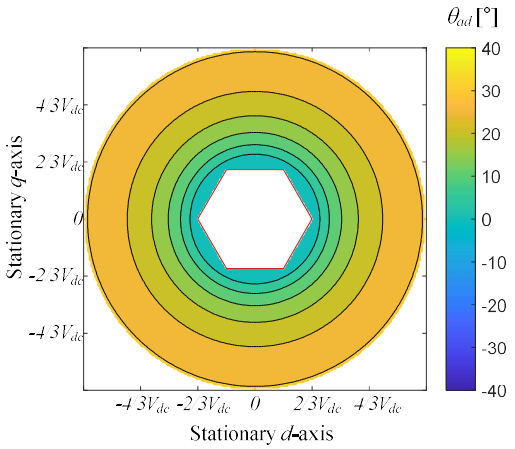

Fig. 12. θ_{ad} according to $\mathbf{v}_{\mathbf{dqs}}^{\mathbf{s}*}$ (AS OVM with α_{sh}=45°).

$$\mathbf{v}_{\mathbf{dqs,O}}^{\mathbf{s}} = \frac{2/3 \cdot V_{dc}}{\| \mathbf{v}_{\mathbf{dqs}}^{\mathbf{s}*} \|} \mathbf{v}_{\mathbf{dqs}}^{\mathbf{s}*} . \tag{19}$$

The voltage difference $\Delta\mathbf{v}_{\mathbf{diff,O}}^{\mathbf{s}}$ is rotated by α_{sh}, and it is added to $\mathbf{v}_{\mathbf{dqs,O}}^{\mathbf{s}}$. α_{sh} is a preset shifting angle, which is a constant value. This modified voltage reference $\mathbf{v}_{\mathbf{dqs}}^{\mathbf{s}**}$ is limited to the edge of the voltage hexagon through MPE OVM. The output voltage of AS OVM, $\mathbf{v}_{\mathbf{dqs,AS}}^{\mathbf{s}}$, can be expressed as

$$\mathbf{v}_{\mathbf{dqs,AS}}^{\mathbf{s}} = \mathrm{MPE}\left(\mathbf{v}_{\mathbf{dqs,O}}^{\mathbf{s}} + \mathbf{R}\left(\mathrm{sgn}(\omega_r) \cdot \alpha_{sh} \right) \Delta\mathbf{v}_{\mathbf{diff,O}}^{\mathbf{s}} \right). \tag{20}$$

As a result, $\mathbf{v}_{\mathbf{dqs,AS}}^{\mathbf{s}}$ is ahead of $\mathbf{v}_{\mathbf{dqs}}^{\mathbf{s}*}$ as much as the angle advance θ_{ad}. Fig. 12 depicts θ_{ad} according to $\mathbf{v}_{\mathbf{dqs}}^{\mathbf{s}*}$ where α_{sh} is set to 45°. In AS OVM, θ_{ad} is kept at a consistent positive angle, regardless of the rotor position. Instead, θ_{ad} is affected by α_{sh} and the magnitude of $\mathbf{v}_{\mathbf{dqs}}^{\mathbf{s}*}$. Since $\| \mathbf{v}_{\mathbf{dqs}}^{\mathbf{s}*} \|$ would be proportional to $\| \mathbf{i}_{\mathbf{dqs,f}}^{\mathbf{r}*} - \mathbf{i}_{\mathbf{dqs,i}}^{\mathbf{r}*} \|$, θ_{ad} will vary according to how severe the reference change is.

The relation between θ_{ad} and $\| \mathbf{v}_{\mathbf{dqs}}^{\mathbf{s}*} \|$ can be analyzed quantitatively. From geometric properties of AS OVM, the following equation is satisfied by the law of sines.

$$\frac{\| \mathbf{v}_{\mathbf{dqs,AS}}^{\mathbf{s}**} \|}{\sin(\alpha_{sh})} = \frac{\| \Delta\mathbf{v}_{\mathbf{diff,O}}^{\mathbf{s}} \|}{\sin(\theta_{ad})} . \tag{21}$$

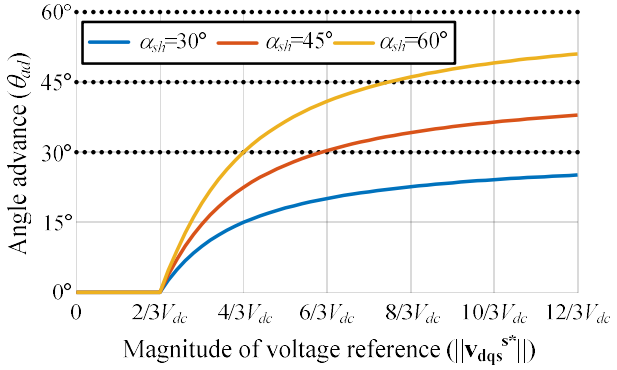

Fig. 13. θ_{ad} according to $\|\mathbf{v}_{dqs}^{s*}\|$ change.

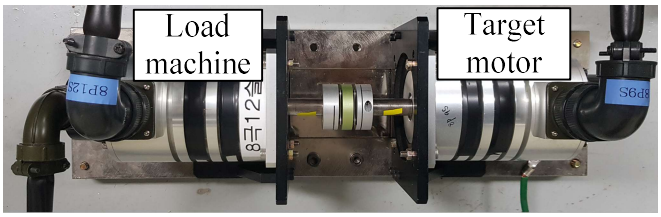

Fig. 14. Motor-generator set used in experimental verification.

TABLE I. Motor parameters

Rated power	1.7	kW
Rated torque	4.5	N·m
Rated current	5.2	A_{rms}
DC-link voltage	311	V_{dc}
Pole/slot	8 / 9	
λ_f	88.4	mWb·t
L_{ds} @ T_e=2 pu	6.3	mH
L_{qs} @ T_e=2 pu	8.5	mH

In addition, $\|\mathbf{v}_{dqs,AS}^{s**}\|$ can be calculated as

$$\|\mathbf{v}_{dqs,AS}^{s**}\| = \sqrt{\left(\frac{2}{3}V_{dc}\right)^2 + \left\|\Delta\mathbf{v}_{diff,O}^{s}\right\|^2 + \frac{4}{3}V_{dc}\left\|\Delta\mathbf{v}_{diff,O}^{s}\right\|\cos(\alpha_{sh})} \,. \quad (22)$$

From (21) and (22), θ_{ad} according to $\|\mathbf{v}_{dqs}^{s*}\|$ can be calculated, as shown in Fig. 13. Above 2/3·V_{dc}, θ_{ad} increases monotonically, as $\|\mathbf{v}_{dqs}^{s*}\|$ is getting larger. When $\|\mathbf{v}_{dqs}^{s*}\|$ is much larger than 2/3·V_{dc}, θ_{ad} asymptotically converges to α_{sh}. Therefore, α_{sh} can be utilized as an upper bound of θ_{ad}.

It should be noted that the d-axis current overshoot is proportional to θ_{ad}. Regarding Fig. 3(c) and Fig. 9, the larger θ_{ad} will result in the more inward convex flux trajectory, which leads to the more d-axis current overshoot. Since α_{sh} determines θ_{ad} as analyzed in Fig. 13, the larger α_{sh} will tend to increase the d-axis current overshoot. Thus, to avoid an unnecessary current overshoot, α_{sh} should be selected among those that give a satisfactory dynamic performance with acceptable d-axis current overshoot. Moreover, since a slight angle shift instead of the minimum distance solution is also effective in achieving the fast-dynamics, a fine tuning of α_{sh} would not be necessary.

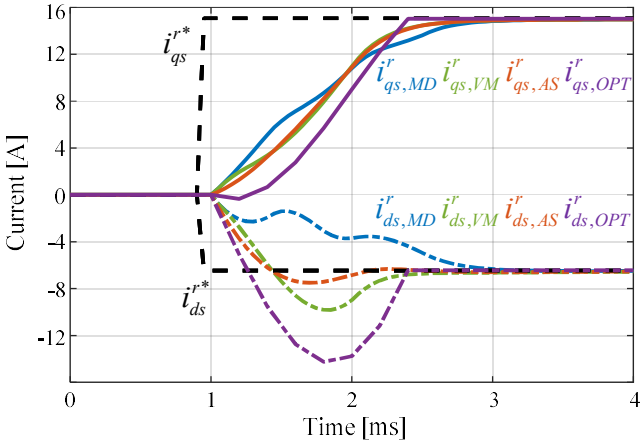

Fig. 15. Current waveforms (Simulation results).

IV. Simulation and Experimental Results

A. Implementation

The simulation and the experiments are conducted to verify the effectiveness of the proposed scheme. MD OVM and VM OVM are also tested for comparison. For a fair comparison, VM OVM combined with MD OVM is implemented. In the experiments, the motor-generator set in Fig. 14 has been used. A 1.7 kW-rated IPMSM is selected as a load machine. The nominal parameters of the target PMSM are listed in TABLE I. The PI-type current regulator, whose bandwidth is set to 500 Hz, has been adopted [20]. To avoid the windup problem in the current regulator, the anti-windup controller gains in Fig. 6 are set as $\mathbf{K_p}^{-1}$. The switching frequency is set to 10 kHz, and the double sampling in a switching period is applied. α_{sh} is set to 45°, otherwise stated.

B. Simulation Results

In the simulation, the ideal motor model with the constant motor parameters in TABLE 1 is used to see the performance of each OVM scheme without other effects, such as spatial harmonics and cross saturation of the motor.

Fig. 15 shows the current waveforms of MD OVM, VM OVM, and the proposed AS OVM. In addition, the minimum distance solution in Fig. 3(b) is also depicted with the purple line as an optimal trajectory. The torque reference of 9 Nm, i.e., 200 % of the rated torque, is applied to the target motor at the moment of θ_r=0°. The load machine regulates the speed at 2500 r/min. While MD OVM has a dilatory current response, VM OVM and AS OVM show smaller settling time thanks to the voltage angle shift. It should be noted that the settling time of VM OVM and AS OVM is very similar to that of the minimum distance solution. It shows that shifting voltage reference angle in advance can provide a quasi-time-optimal solution at the rapid current reference change.

Fig. 16(a)-(c) depict the corresponding flux trajectories of each OVM method. The time interval between each stamp is 200 μs, which is four sampling periods. In Fig. 16(a), MD OVM shows the least angle shift and the longest settling time. In contrast, VM OVM shows a noticeable voltage angle shift, which enhances the settling time. However, since the degree of

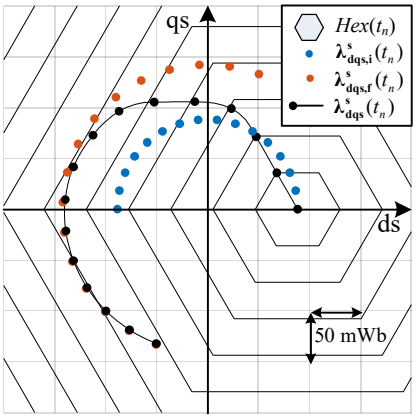

(a)

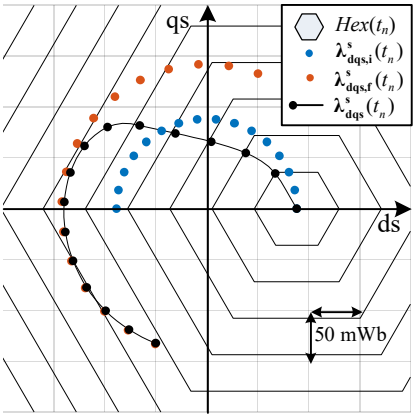

(b)

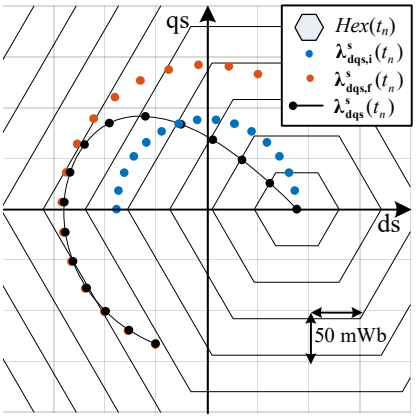

(c)

Fig. 16. Flux trajectories (Simulation results). (a) MD OVM. (b) VM OVM. (c) Proposed AS OVM.

the voltage angle shift is affected by the edges of the voltage hexagon, the flux trajectory suddenly changes its direction, which results in the substantial *d*-axis current overshoot. Unlike the conventional methods, the proposed AS OVM shows the smooth flux trajectory and less *d*-axis current overshoot without losing the dynamic performance. In Fig. 16(a)-(c), it can be noticed that the stamps of $\boldsymbol{\lambda}^s_{dqs}(t_n)$ have a misalignment with the edges of $Hex(t_n)$. It is due to the resistive voltage drop, which has not been considered in (1).

Fig. 17(a) and (b) show the effect of α_{sh} variation in the proposed AS OVM. In Fig. 17(a), 200% of the rated torque is applied to the motor under test, while changing α_{sh} from 10° to 90°. As in Fig. 15, the load torque is applied where the rotor position is at 0°. As analyzed in Section II., α_{sh} variation barely changes the settling time, except for the case of α_{sh}=10°. It indicates that setting α_{sh} less than 30° would not be enough for reducing the settling time. However, α_{sh} affects the *d*-axis current overshoot significantly. In the case of α_{sh}=90°, *d*-axis current exceeds -13 A in maximum, and it is unnecessary for the fast response. The case of α_{sh}=45° provides the reasonable *d*-axis current overshoot with the fast settling time. Moreover, AS OVM with α_{sh}=45° can be easily implemented, since $\mathbf{R}(\alpha_{sh})$ is simplified as $\frac{1}{\sqrt{2}}\begin{bmatrix}1 & -1\\ 1 & 1\end{bmatrix}$.

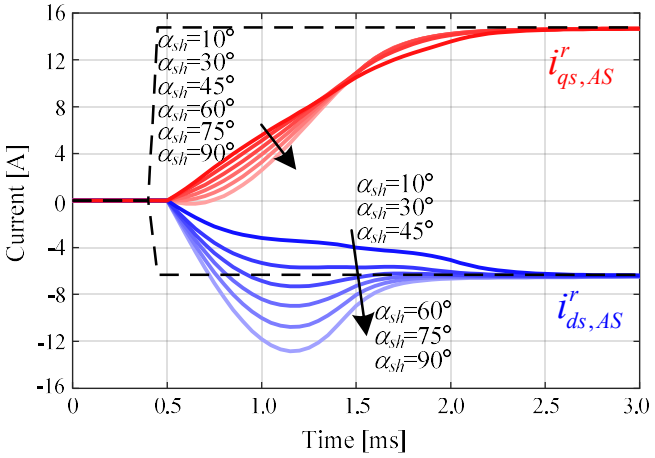

(a)

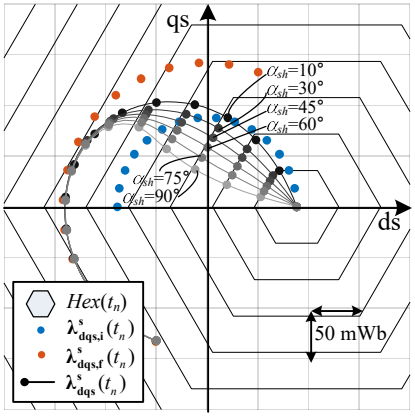

(b)

Fig. 17. Current waveforms according to α_{sh} variation (Simulation results). (a) Time domain. (b) Flux trajectory.

The settling-time-invariance can be confirmed by the flux trajectories in Fig. 17(b). Except for the case of α_{sh}=10°, the stamps of the flux trajectories are at the boundary of each $Hex(t_n)$. The cases of α_{sh}=30° and α_{sh}=45° correspond to the outward convex time optimal solution in Fig. 3(c), and those of α_{sh}=75° and α_{sh}=90° would correspond to the inward convex time optimal solution.

Fig. 18(a)-(c) depict the overlapped current waveforms at various θ_r. The rotor angle where the torque reference varies is changed from zero to 50° with 10° steps. In Fig. 18(a), MD

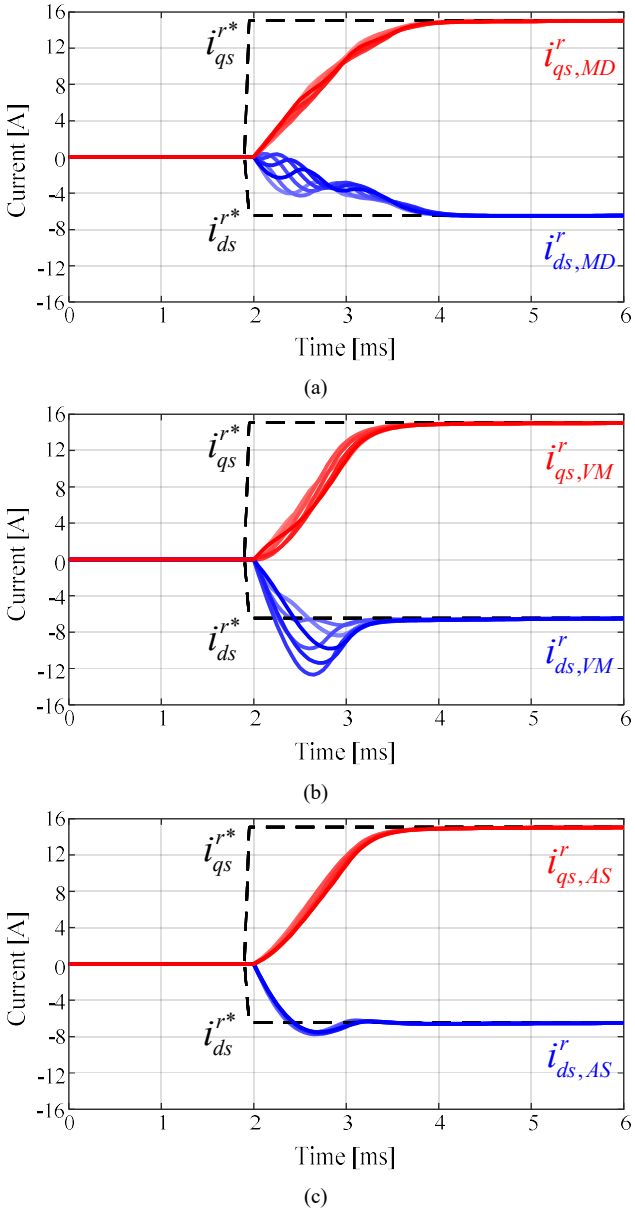

Fig. 18. Current waveforms at various θ_r (Simulation results). (a) MD OVM. (b) VM OVM. (c) Proposed AS OVM.

OVM shows a moderate dynamic performance regardless of the rotor position. In addition, MD OVM has an irregular current response when the step torque reference is applied at different rotor angles, especially in the *d*-axis current waveforms. In Fig. 18(b), the irregular *d*-axis current waveform is getting severe in VM OVM. Since VM OVM has an overshoot in transient *d*-axis current, the nonuniform current response may affect the maximum current rating or the demagnetization limit of PMSM. In contrast, the proposed AS OVM keeps the fast-dynamic performance regardless of the rotor position change. Furthermore, the overshoot of *d*-axis current is also well-suppressed in every rotor position.

C. Experimental Results

In Fig. 19(a)-(c), the experimental results of step torque response are shown. As in the simulation, 200 % of the rated torque has been applied when θ_r=0°. The rotor speed is regulated as 2500 r/min by the load machine. In Fig. 19(a), the

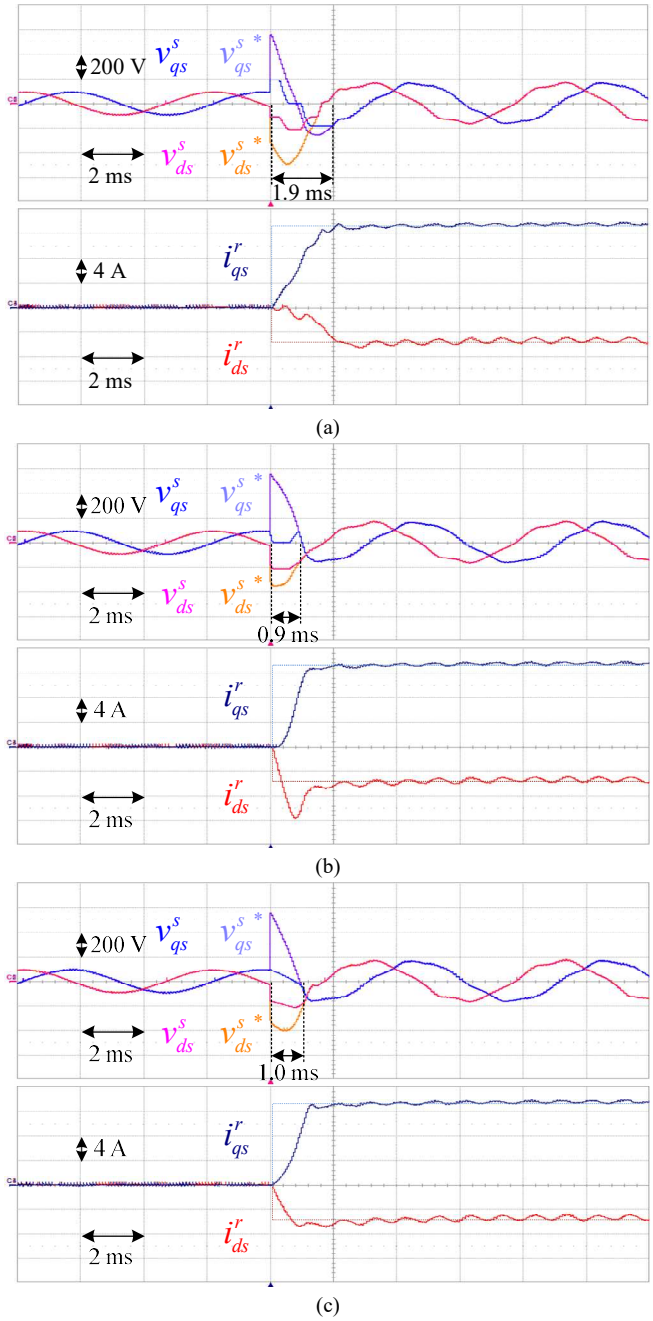

Fig. 19. Voltage and current waveforms under load change at θ_r=0° (Experimental results). (a) MD OVM. (b) VM OVM. (c) Proposed AS OVM.

voltage reference remains in OVM region for 1.9 ms after the load change. In Fig. 19(b), VM OVM shows a better dynamic performance reducing the settling time to 0.9 ms. However, a massive *d*-axis current overshoot, almost twice the current reference, occurs during the transient state. In Fig. 19(c), the proposed AS OVM has a settling time comparable to that of VM OVM with negligible overshoot in *d*-axis current. Unlike the simulation results with the ideal motor model, the current and voltage waveforms in Fig. 19(a)-(c) have the ripple term even at the steady state due to the spatial harmonics of the motor.

Instead of the flux trajectory, which is not easy to be measured, the Lissajous waveforms of voltage references are

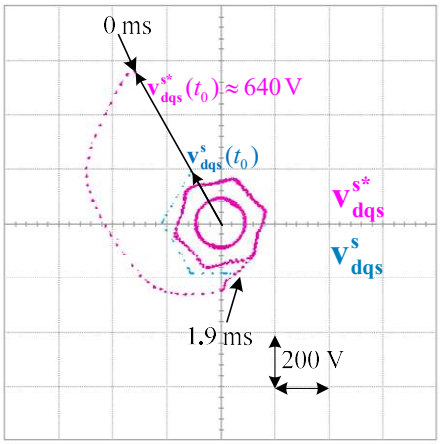

(a)

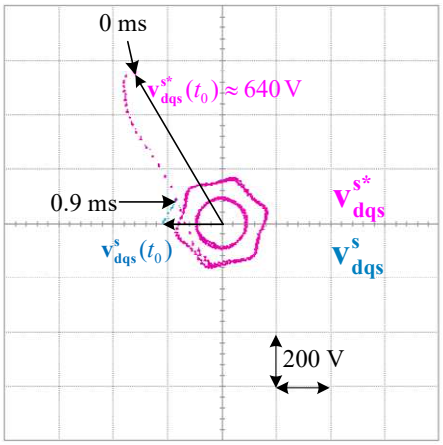

(b)

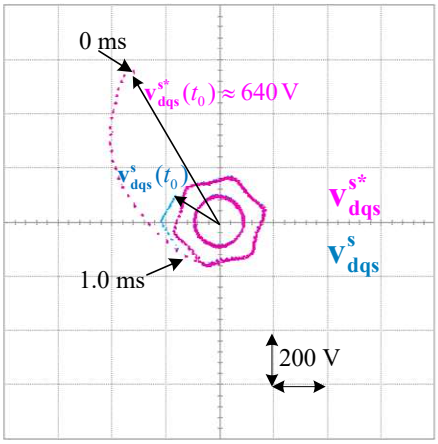

(c)

Fig. 20. Lissajous waveforms of $\mathbf{v}^{s*}_{dqs}$ and $\mathbf{v}^{s}_{dqs}$ (Experimental results). (a) MD OVM. (b) VM OVM. (c) Proposed AS OVM.

shown in Fig. 20(a)-(c). The magenta and blue stamps represent $\mathbf{v}^{s*}_{dqs}$ and $\mathbf{v}^{s}_{dqs}$ at each sampling period, respectively. Regardless of the OVM methods, the first voltage reference after the load change, i.e., $\mathbf{v}^{s*}_{dqs}(t_0)$, soars over 600 V, which is more than thrice the maximum synthesizable stator voltage, $2/3 \cdot V_{dc}$. In Fig. 20(a), MD OVM limits $\mathbf{v}^{s}_{dqs}$ to the edge of the voltage hexagon without a meaningful voltage angle shift. In Fig. 20(b), VM OVM results in an excessive voltage angle shift, which leads to

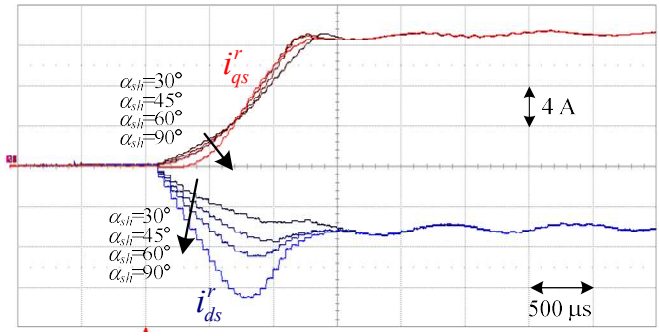

Fig. 21. Current waveforms at various α_{sh} (Experimental results).

the considerable *d*-axis current overshoot. In contrast, in Fig. 20(c), the proposed AS OVM modifies the voltage reference with an adequate angle advance, so that the fast-dynamics are achieved with less *d*-axis current overshoot.

Fig. 21 shows the current waveforms at various α_{sh}. The twice the rated torque is applied to the motor under test, while α_{sh} is changed from 30° to 90°. It can be noticed that the excessive α_{sh} barely affects the settling time, but it only increases the *d*-axis current overshoot. Regarding the current overshoot and the ease of implementation, α_{sh} is set to 45° in the rest of experiments as in the simulation.

Fig. 22(a)-(c) depict the overlapped current waveforms for various rotor positions. In each figure, the rotor position at the load change is set from zero to 50° in 10° steps, as those in Fig. 18. The tendency of each method is quite similar to the simulation results in Fig. 18. With MD OVM, the currents are settled within more than 2 ms, while VM OVM reduces the settling time to almost 1 ms. However, the overshoot of the d-axis current in VM OVM is severe and irregular. Within the proposed method, not only is the fast-dynamics secured as in VM OVM, but the overshoot of *d*-axis current is also well-regulated at the reference value. These experimental results demonstrate that the proposed AS OVM is still feasible in real PMSMs where the flux saturation and spatial harmonics are present.

To see the effectiveness of the proposed method at various operating conditions, the experimental results at various speeds and torque references are shown in Fig. 23(a)-(c). In Fig. 23(a), (b), and (c), 200 %, 150 %, and 100 % of rated torque are applied to the target motor, while the rotor speeds are set to 1500 r/min, 2500 r/min, and 3000 r/min, respectively. In each case, the rotor position is changed from zero to 50° in 10° steps, and their waveforms are overlapped in each plot. In all cases, the proposed AS OVM provides uniform current trajectories regardless of the rotor position. Also, the *d*-axis current overshoot is well-suppressed, while keeping the fast current response.

V. Conclusion

This paper proposes a dynamic OVM scheme which is robust to rotor angle variation. Unlike the other OVMs that focus on maximizing the voltage utilization, the proposed method puts more importance on maintaining the proper voltage direction. In addition, the proposed OVM scheme is designed assuming

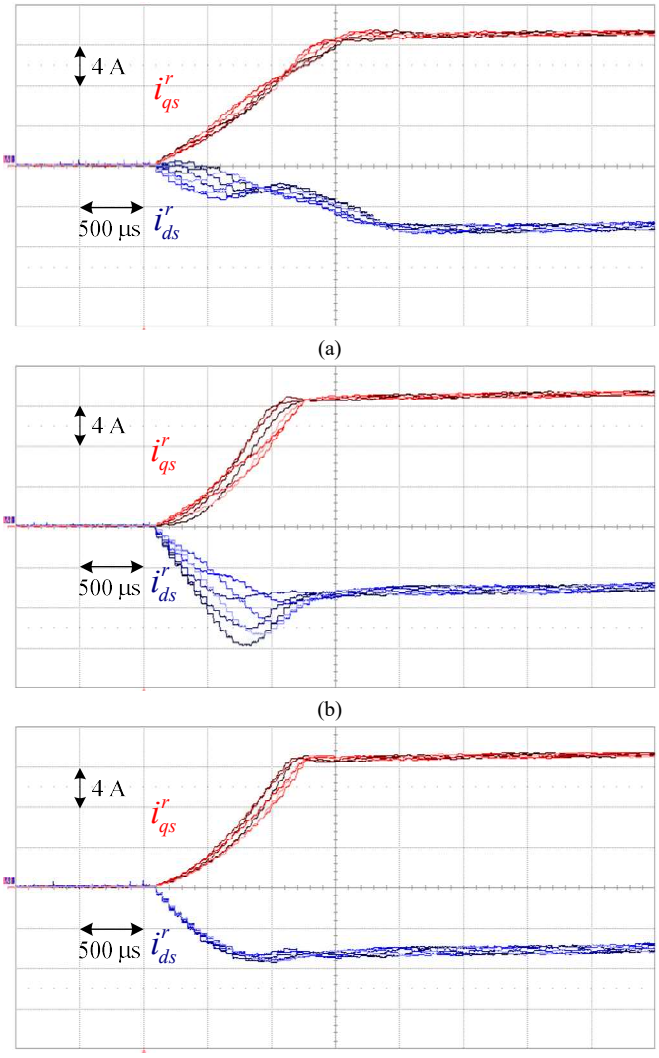

Fig. 22. Current waveforms at various θ_r (Experimental results). (a) MD OVM. (b) VM OVM. (c) Proposed AS OVM.

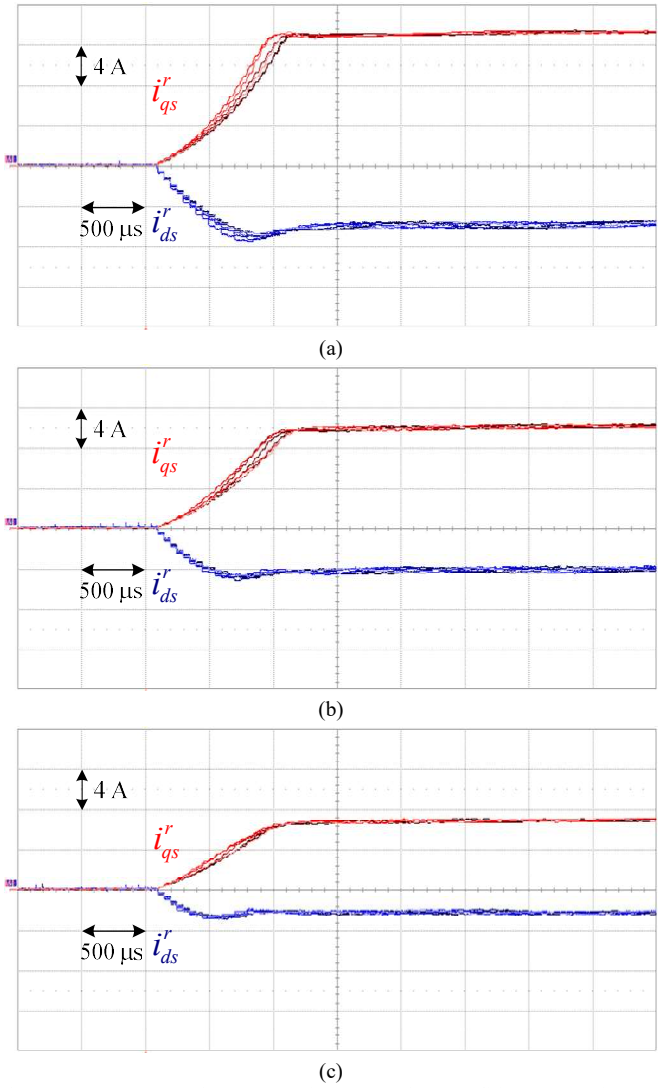

Fig. 23. Current waveforms at various operating conditions (Experimental results). (a) 200 % torque at 1500 r/min. (b) 150 % torque at 2500 r/min. (c) Rated torque at 3000 r/min.

the cooperation with the standard PI-current regulator. Hence, it does not require an additional transition process from the linear region to OVM region. Thanks to the proposed method, the consistent dynamic performance in OVM region regardless of the rotor position has been achieved. Furthermore, keeping the fast dynamic performance, the proposed method reduces the overshoot of *d*-axis current and makes it predictable, which is known to be the drawback of most OVMs with fast-dynamics. The simulation and experimental results with a 1.7 kW-rated IPMSM verify the feasibility of the proposed method.

APPENDIX

Eq. (9) can be divided into the following inequalities.

$$\frac{1}{3}\Delta\theta_{r,opt}{}^2 \le a^2+b^2-2ab\cos\left(\delta+\Delta\theta_{r,opt}\right), \tag{23}$$

$$a^2+b^2-2ab\cos\left(\delta+\Delta\theta_{r,opt}\right) \le \frac{4}{9}\Delta\theta_{r,opt}{}^2, \tag{24}$$

where

$$0 < a = \omega_r \frac{\left\|\boldsymbol{\lambda}_{\mathbf{dqs,f}}^{\mathbf{r*}}\right\|}{V_{dc}} < \frac{1}{\sqrt{3}}, \tag{25}$$

$$0 < b = \omega_r \frac{\left\|\boldsymbol{\lambda}_{\mathbf{dqs,i}}^{\mathbf{r*}}\right\|}{V_{dc}} < \frac{1}{\sqrt{3}}. \tag{26}$$

Eq. (23) can be rewritten as follows.

$$2ab\cos\left(\delta+\Delta\theta_{r,opt}\right) < a^2+b^2-\frac{1}{3}\Delta\theta_{r,opt}{}^2. \tag{27}$$

Since $-1 \le \cos(x) \le 1$ for an arbitrary real number x, the following inequality should be satisfied.

$$-2ab < a^2+b^2-\frac{1}{3}\Delta\theta_{r,opt}{}^2. \tag{28}$$

Applying (25) and (26), $\Delta\theta_{r,opt}$ satisfies the following condition.

$$\Delta\theta_{r,opt} < \sqrt{3}(a+b) < 2\,. \tag{29}$$

REFERENCES

[1] J. Holtz, W. Lotzkat and A. M. Khambadkone, "On continuous control of PWM inverters in the overmodulation range including the six-step mode," in *IEEE Transactions on Power Electronics*, vol. 8, no. 4, pp. 546-553, Oct. 1993.

[2] S. Bolognani and M. Zigliotto, "Novel digital continuous control of SVM inverters in the overmodulation range," in *IEEE Transactions on Industry Applications*, vol. 33, no. 2, pp. 525-530, March-April 1997.

[3] A. M. Hava, R. J. Kerkman, and T. A. Lipo, "Carrier-based PWM-VSI overmodulation strategies: analysis, comparison, and design," in *IEEE Transactions on Power Electronics*, vol. 13, no. 4, pp. 674-689, July 1998.

[4] J. Seok, J. Kim and S. -K. Sul, "Overmodulation strategy for high-performance torque control," in *IEEE Transactions on Power Electronics*, vol. 13, no. 4, pp. 786-792, July 1998.

[5] B. Bae and S. -K. Sul, "A novel dynamic overmodulation strategy for fast torque control of high-saliency-ratio AC motor," in *IEEE Transactions on Industry Applications*, vol. 41, no. 4, pp. 1013-1019, July-Aug. 2005.

[6] S. Lerdudomsak, S. Doki and S. Okuma, "Voltage limiter calculation method for fast torque response of IPMSM in overmodulation range," *2009 35th Annual Conference of IEEE Industrial Electronics*, Porto, Portugal, 2009, pp. 1383-1388.

[7] J. Richter and M. Doppelbauer, "Predictive Trajectory Control of Permanent-Magnet Synchronous Machines With Nonlinear Magnetics," in *IEEE Transactions on Industrial Electronics*, vol. 63, no. 6, pp. 3915-3924, June 2016.

[8] S. Lerdudomsak, M. Kadota, S. Doki and S. Okuma, "Novel Techniques for Fast Torque Response of IPMSM Based on Space-Vector Control Method in Voltage Saturation Region," *IECON 2007 - 33rd Annual Conference of the IEEE Industrial Electronics Society*, Taipei, Taiwan, 2007, pp. 1015-1020.

[9] A. Sarajian *et al.*, "Overmodulation Methods for Modulated Model Predictive Control and Space Vector Modulation," in *IEEE Transactions on Power Electronics*, vol. 36, no. 4, pp. 4549-4559, April 2021.

[10] J. Choi and S. -K. Sul, "Generalized solution of minimum time current control in three-phase balanced systems," in *IEEE Transactions on Industrial Electronics*, vol. 45, no. 5, pp. 738-744, Oct. 1998.

[11] S. Bolognani, M. Tomasini, L. Tubiana and M. Zigliotto, "DSP-based time optimal current control for high dynamic IPM motor drives," *2004 IEEE 35th Annual Power Electronics Specialists Conference (IEEE Cat. No.04CH37551)*, Aachen, Germany, 2004, pp. 2197-2203 Vol.3.

[12] J. S. Lee, R. D. Lorenz and M. A. Valenzuela, "Time-Optimal and Loss-Minimizing Deadbeat-Direct Torque and Flux Control for Interior Permanent-Magnet Synchronous Machines," in *IEEE Transactions on Industry Applications*, vol. 50, no. 3, pp. 1880-1890, May-June 2014.

[13] W. Wang, M. Du and K. Wei, "Rapid Torque Rising of PMSM by Directly Chasing Rotating Flux Linkage Vector," in *IEEE Journal of Emerging and Selected Topics in Power Electronics*, vol. 9, no. 4, pp. 4384-4394, Aug. 2021.

[14] H. Cho, Y. Kwon and S. -K. Sul, "Time-Optimal Voltage Vector Transition Scheme for Six-Step Operation of PMSM," in *IEEE Transactions on Power Electronics*, vol. 36, no. 5, pp. 5724-5735, May 2021.

[15] Y. Kwon, S. Kim and S. -K. Sul, "Voltage Feedback Current Control Scheme for Improved Transient Performance of Permanent Magnet Synchronous Machine Drives," in *IEEE Transactions on Industrial Electronics*, vol. 59, no. 9, pp. 3373-3382, Sept. 2012.

[16] Y. Kwon, S. Kim and S. -K. Sul, "Six-Step Operation of PMSM With Instantaneous Current Control," in *IEEE Transactions on Industry Applications*, vol. 50, no. 4, pp. 2614-2625, July-Aug. 2014.

[17] A. M. Hava, S. -K. Sul, R. J. Kerkman and T. A. Lipo, "Dynamic overmodulation characteristics of triangle intersection PWM methods," in *IEEE Transactions on Industry Applications*, vol. 35, no. 4, pp. 896-907, July-Aug. 1999.

[18] J. Yun, J. Yoo, H. -S. Jung and S. -K. Sul, "Simple Overmodulation Scheme for Improved Dynamic Performance of IPMSM," *2020 IEEE Transportation Electrification Conference & Expo (ITEC)*, Chicago, IL, USA, 2020, pp. 901-905.

[19] J. Yoo and S. -K. Sul, "Dynamic Overmodulation for Improved Current Regulation of PMSM," *2020 IEEE Energy Conversion Congress and Exposition (ECCE)*, Detroit, MI, USA, 2020, pp. 5368-5374.

[20] S. -K. Sul, *Control of Electric Machine Drive Systems*. Hoboken, NJ, USA: Wiley, 2010.

Jiwon Yoo (S'17) was born in Seoul, South Korea in 1990. He received the B.S. degree in electrical engineering from Seoul National University, Seoul, South Korea in 2017, where he is currently pursuing the Ph.D. degree in electrical engineering. From 2014 to 2017, He was a Research Engineer with Seoho Electric Company, Anyang, South Korea. His current research interests include power electronics, control of electric machines, power semiconductors, and sensorless drives.

He was the recipient of the Best Paper Award First Prize at 2019 International Conference on Power Electronics (ICPE-Busan/ECCE-Asia) and the Best Paper Award at 2020 International Power Electronics and Motion Control Conference (IPEMC-Nanjing/ECCE-Asia).

Seung-Ki Sul (S'78–M'87–SM'98–F'00) received the B.S., M.S., and Ph.D. degrees in electrical engineering from Seoul National University, Seoul, South Korea, in 1980, 1983, and 1986, respectively. From 1986 to 1988, he was an Associate Researcher with the Department of Electrical and Computer Engineering, University of Wisconsin, Madison, WI, USA. From 1988 to 1990, he was a Principal Research Engineer with LG Industrial Systems Company, South Korea. Since 1991, he has been a faculty member with the School of Electrical and Computer Engineering, Seoul National University, where he is currently a Professor. He has authored or coauthored more than 150 IEEE journal papers and a total of more than 340 international conference papers in the area of power electronics. His current research interests include position sensorless control of electrical machines, electric/hybrid vehicles and ship drives, and power-converter circuits based on SiC MOSFET.

Dr. Sul was the Program Chair of IEEE Power Electronics Specialists Conference in 2006 and the General Chair of IEEE International Conference on Power Electronics and ECCE-Asia in 2011. From 2011 to 2014, he was the Editor-in-Chief for the Journal of Power Electronics, an SCIE-registered journal published by the Korean Institute of Power Electronics (KIPE), Seoul, South Korea. For the year 2015, he was the President of KIPE. He was simultaneously the recipient of the 2015 IEEE Transaction 1st and 2nd Paper Awards on Industrial Application. He was also the recipient of the 2016 Outstanding Achievement Award of the IEEE Industrial Application Society. He was also selected as the recipient of the 2017 Newell award sponsored by IEEE Power Electronics Society. For the last 40 years of R &D experience, he involved in over 150 industry-sponsored collaboration projects in the area of elevator drive, steel mill plant, home appliance, PCS of renewables, electric/hybrid vehicles, and ship propulsion.